

# Infrared surface phonon nanospectroscopy of an interacting dielectric-particle–dielectric-substrate dimer using fast electrons

Elliot K. Beutler <sup>1</sup>, Maureen J. Lagos,<sup>2</sup> and David J. Masiello <sup>1,\*</sup>

<sup>1</sup>*Department of Chemistry, University of Washington, Seattle, Washington 98195, United States*

<sup>2</sup>*Department of Materials Science and Engineering, McMaster University, Hamilton, Ontario L8S 4M1, Canada*



(Received 31 January 2021; accepted 15 April 2021; published 23 April 2021)

Refinements in energy monochromation and aberration correction in state-of-the-art scanning transmission electron microscopes has opened access to the far infrared regime for spectroscopic characterization at the nanoscale. At these low energies, the dielectric environment, such as a dielectric slab adjacent to the target specimen, may no longer play a passive role in the spectrum. Instead, the environment may itself host resonances that mix with those of the target and complicate interpretation of its spectral responses. This paper explores a theoretical description of the coupling between the collective vibrational surface modes of a dielectric particle and dielectric slab of varying thickness for the purpose of elucidating the interacting phononic excitations in dielectric materials typical of inelastic electron scattering measurements in the infrared. Dynamical coordinates and a governing Hamiltonian are rigorously defined in the quasistatic limit to account for phonon mode mixing and forcing by an aloof electron probe, which travels along a grazing trajectory, parallel to the dielectric slab. As the spectral window of interrogation by fast electron probes has been extended down to thermal energies with unprecedented meV energy resolution, theoretical models like that presented herein are crucial for accurate interpretation of experimental data.

DOI: [10.1103/PhysRevB.103.165418](https://doi.org/10.1103/PhysRevB.103.165418)

## I. INTRODUCTION

Recent advances in electron microscopy have enabled unprecedented spatial imaging at the atomic scale combined with refined spectroscopic resolution of inelastic scattering processes at increasingly low energy due to improved monochromation and aberration correction of the incident electron beam [1–6]. These developments have paved the way for examination of progressively lower energy excitations, including the molecular vibrations of organic and biological compounds [7,8], as well as surface and bulk phonons hosted by macroscopic samples, thin films, individual nanoparticles, and nanoparticle assemblies of varying morphologies, none of which had been previously characterized by electron energy loss spectroscopy (EELS) [9–15]. Unlike a plane-wave light source, a uniformly moving electron carries an evanescent field akin to the broad spectrum white light source produced by synchrotron radiation. When utilized as a spectroscopic probe, it is capable of characterizing target excitations across a broad spectral range, from low-energy collective surface and bulk resonances to valence electronic transitions to core-loss events at high energy.

As the available spectroscopic window of the electron microscope has extended ever lower in energy, now down to thermal energies ( $\sim 25$  meV), the vibrational modes probed by the electron beam on individual nanoparticles become apparent [2,10,16,17]. In this regime, dielectric nanoparticles and their planar dielectric substrates may be coresonant.

When placed in proximity, independent nanoparticle and substrate excitations are able to appreciably couple in the near field, and it is the composite nanoparticle-substrate assembly that is ultimately interrogated by the electron beam. The consequences of such phonon mode hybridization may be perceptible through inelastic electron scattering, producing a rich and nuanced spectrum deserving of an in-depth analysis.

Previous work [18,19] has explored substrate effects in electron-scattering measurements of nanoparticle targets, particularly how their presence can renormalize the eigenfrequencies of the target's excited surface modes. Others have investigated the potential for energy transfer facilitated by the spectral overlap of a nanoparticle's surface mode resonances with the band-gap energies of its supporting semiconductor substrate, an adsorbate molecule, or an adjacent nanoparticle [20–26].

In this paper, we present a theoretical model-based approach to interpreting the measured scattering probability of a composite dielectric nanoparticle-substrate dimer system for a grazing electron beam geometry, showcasing that a consideration of only the nanoparticle's renormalized eigenmodes is insufficient in interpreting the resulting scattering signal when both the sample and substrate materials are dispersive in the same spectral region. For simplicity, we will consider a spherical nanoparticle target positioned directly adjacent to the surface of a dielectric slab, where both the particle and slab host nearly coresonant surface mode responses in the infrared. We then investigate the resulting interaction between the electron probe, nanoparticle, and slab encoded in the spectrum of the scattered electron beam.

\*masiello@uw.edu

We begin by working within a classical dielectric formalism and construct a system Hamiltonian after defining time-dependent coordinates for the oscillatory surface modes of both the sphere and substrate. This allows for a characterization of the energies of interaction and associated forces between the electron probe, nanoparticle, and substrate at the level of the equations of motion. We then examine the linear response of the dielectric sphere, deriving its effective polarizability in the presence of a substrate of varying depths, by solving the coupled equations of motion in Fourier space. Correspondingly, we also derive the linear response of the semi-infinite dielectric slab in the presence of the sphere. This permits an exploration of how the system evolves in response to an external perturbing field when the distance between the sphere and substrate surface is altered and when the thickness of the supporting substrate is varied. The near-field interactions between the surface modes on the sphere and substrate are visualized with the aid of induced electric near-field profiles, simulated using plane-wave excitation with specific polarization. Finally, we derive an expression of the sphere-substrate dimer's corresponding scattering probability for a dielectric slab of varying thicknesses and compare the results to a simulated electron-scattering experiment based on a numerical solution of Maxwell's equations. In both cases, we consider an aloof grazing trajectory, with the path of the electron beam oriented parallel to the thin film surface and traveling entirely in vacuum, avoiding the excitation of bulk phonon mode resonances [15]. Excellent agreement between simulations and the developed model highlights the importance of the substrate (which we henceforth refer to more generally as a dielectric slab) as a separate dynamical component that can strongly modify the infrared responses of the nanoparticle target.

## II. SURFACE PHONON MODES OF THE SPHERE AND SUBSTRATE AND THEIR GENERALIZED COORDINATES

To characterize the electromagnetic surface modes hosted by a finite dielectric sphere and slab, the latter modeled as a thin film extended infinitely along  $x, z$  directions and of finite thickness  $-d \leq y \leq 0$  in  $y$ , we begin at the level of the potentials and derive their auxiliary Green's functions. In general, for a material described by a dielectric function that is local in space but not in time, its response to an external perturbing charge distribution  $\rho$  is determined by the time-dependent Poisson equation,

$$-\nabla \cdot \int_{-\infty}^t dt' \varepsilon(\mathbf{x}; t - t') \nabla \Phi(\mathbf{x}, t') = 4\pi \rho(\mathbf{x}, t), \quad (1)$$

in the quasistatic limit with Green's function  $G$  satisfying

$$\begin{aligned} -\nabla \cdot \int_{-\infty}^t dt' \varepsilon(\mathbf{x}; t - t'') \nabla G(\mathbf{x}, \mathbf{x}'; t'' - t') \\ = 4\pi \delta(\mathbf{x} - \mathbf{x}') \delta(t - t'). \end{aligned} \quad (2)$$

By allowing the upper bound of the integral to approach infinity as the perturbation of the point source extends from the infinite past into the infinite future, Eq. (2) may be Fourier transformed in  $t - t'$  to produce  $-\nabla \cdot \tilde{\varepsilon}(\mathbf{x}, \omega) \nabla \tilde{G}(\mathbf{x}, \mathbf{x}'; \omega) = 4\pi \delta(\mathbf{x} - \mathbf{x}')$ . Exploiting the orthogonality of the spherical har-

monics and the cylindrical Bessel functions, and applying by standard procedure [27–29] the appropriate boundary conditions, yields the following Green's functions for the dielectric sphere and the dielectric finite-thickness slab in spherical and cylindrical coordinates, respectively:

$$\begin{aligned} \tilde{G}_1(\mathbf{x}, \mathbf{x}'; \omega) \\ = \frac{1}{|\mathbf{x} - \mathbf{x}'|} - \sum_{\ell m} \frac{4\pi}{2\ell + 1} \frac{a^{2\ell+1}}{r'^{\ell+1} r^{\ell+1}} Y_{\ell m}(\theta, \phi) \\ \times Y_{\ell m}^*(\theta', \phi') \tilde{\beta}_{\ell}(\omega), \end{aligned} \quad (3)$$

$$\begin{aligned} \tilde{G}_2(\mathbf{x}, \mathbf{x}'; \omega) \\ = \frac{1}{|\mathbf{x} - \mathbf{x}'|} - \sum_{n=-\infty}^{\infty} e^{in(\phi-\phi')} \int_0^{\infty} dk J_n(k\rho) \\ \times J_n(k\rho') e^{-k(y+y')} \tilde{\zeta}_k(\omega), \end{aligned} \quad (4)$$

when the source ( $\mathbf{x}'$ ) and observation ( $\mathbf{x}$ ) points are in the same region outside of the dielectric. Embedded within these Green's functions are the geometric surface response functions,

$$\tilde{\beta}_{\ell}(\omega) = \frac{\ell(\tilde{\varepsilon}_1(\omega) - 1)}{\ell(\tilde{\varepsilon}_1(\omega) + 1) + 1}, \quad (5)$$

$$\tilde{\zeta}_k(\omega) = \frac{(\tilde{\varepsilon}_2(\omega)^2 - 1)(1 - e^{-2kd})}{(\tilde{\varepsilon}_2(\omega) + 1)^2 - (\tilde{\varepsilon}_2(\omega) - 1)^2 e^{-2kd}}, \quad (6)$$

expressed in terms of the dielectric functions  $\tilde{\varepsilon}_{1,2}(\omega)$  of the sphere (1) and slab (2) in a vacuum environment (i.e.,  $\varepsilon_b = 1$ ). The surface resonance conditions of each are determined by the pole structure of Eqs. (5) and (6). It is therefore apparent that the sphere hosts an infinite number of discrete surface resonances, indexed by integer  $\ell$ , while the slab simultaneously hosts a pair of surface resonances, which evolve continuously with changing  $kd$  [30]. In Eqs. (3) and (4), the first term is the Green's function for the inhomogeneous Poisson equation, which accounts for the presence of the point source. The second, containing  $\tilde{\beta}_{\ell}$  and  $\tilde{\zeta}_k$ , are the induced Green's functions  $G_{\text{sph}}$  and  $G_{\text{slab}}$  of the dielectric objects. Here,  $a$  is the sphere radius and  $d$  is the substrate thickness, and the latter extends along dimension  $y$ .  $r, \theta$ , and  $\phi$  are the respective radial, polar, and azimuthal coordinates, and the cylindrical radial coordinate  $\rho = \sqrt{x^2 + z^2}$ .

Considering the time-domain representations of the response functions permits a definition for the dynamic induced potentials  $\Phi_{\text{sph}}$  and  $\Phi_{\text{slab}}$  as the product of a space-dependent mode function and time-dependent amplitude decomposition [31]. We write

$$\begin{aligned} \Phi_{\text{sph}}(\mathbf{x}, t) &= \int d\mathbf{x}' dt' G_{\text{sph}}(\mathbf{x}, \mathbf{x}'; t - t') \rho(\mathbf{x}', t') \\ &= \sum_{\ell m} f_{\ell m}(\mathbf{x}) u_{\ell m}(t), \end{aligned} \quad (7)$$

$$\begin{aligned} \Phi_{\text{slab}}(\mathbf{x}, t) &= \int d\mathbf{x}' dt' G_{\text{slab}}(\mathbf{x}, \mathbf{x}'; t - t') \rho(\mathbf{x}', t') \\ &= \sum_{n=-\infty}^{\infty} \int_0^{\infty} dk \Lambda_n(k, \mathbf{x}) Q_n(k, t). \end{aligned} \quad (8)$$

The time-dependent dynamical coordinates are defined as

$$u_{\ell m}(t) = -\sqrt{12\pi}a^3 \frac{2\ell+1}{e^2} \int d\mathbf{x}' dt' f_{\ell m}^*(\mathbf{x}') \rho(\mathbf{x}', t') \beta_{\ell}(t-t'), \quad (9)$$

$$Q_n(k, t) = -\frac{1}{(ek^2)^2} \int d\mathbf{x}' dt' \Lambda_n^*(k, \mathbf{x}') \rho(\mathbf{x}', t') \zeta_k(t-t'), \quad (10)$$

and the mode functions are defined as

$$f_{\ell m}(\mathbf{x}) = -\sqrt{\frac{4\pi}{3}} \frac{e}{2\ell+1} \frac{a^{\ell-1}}{r^{\ell+1}} Y_{\ell m}(\theta, \phi), \quad (11)$$

$$\Lambda_n(k, \mathbf{x}) = -ek^2 e^{in\phi} J_n(k\rho) e^{-ky}. \quad (12)$$

The coordinates  $u_{\ell m}$  and  $Q_n$  represent a collective time-dependent amplitude response of the charge carriers of the sphere and slab, the dynamics of which are determined by the response functions  $\beta_{\ell}$  and  $\zeta_k$ , and the time-dependent charge distribution  $\rho$ . The mode functions  $f_{\ell m}$  and  $\Lambda_n$  describe the spatial profile of the  $\ell, m, n$  mode responses.

For the particular case of a semi-infinite slab, i.e., in the limit that the slab thickness  $d \rightarrow \infty$ , its response function surrenders all dependence on  $k$ ,  $\zeta_k(\omega) \rightarrow \zeta(\omega) = (\tilde{\epsilon}_2(\omega) - 1)/(\tilde{\epsilon}_2(\omega) + 1)$ , and the induced Green's function in the time domain reduces to  $G_{\text{slab}} = -\zeta(t-t')/|\mathbf{x} - \bar{\mathbf{x}}'|$ . In Cartesian coordinates, the vector  $\bar{\mathbf{x}}' = (x', -y', z')$  specifies the position of the fictitious image charge generated in the dielectric slab. Then we utilize a Lorentz dielectric model  $\tilde{\epsilon}_i(\omega) = \epsilon_{\infty, i} + \omega_{p, i}^2/(\omega_i^2 - \omega^2 - i\gamma_i\omega)$  to describe the sphere and substrate bulk responses, where  $i = 1, 2$ ,  $\beta_{\ell}$  and  $\zeta$  are well defined in the time domain. Explicitly,

$$\beta_{\ell}(t-t') = \frac{\tilde{\omega}_{\ell}^2}{\Omega_{\ell}} e^{-\gamma_{\ell}(t-t')/2} \sin \Omega_{\ell}(t-t'), \quad (13)$$

$$\zeta(t-t') = \frac{\tilde{\omega}_s^2}{\Omega_s} e^{-\gamma_s(t-t')/2} \sin \Omega_s(t-t'), \quad (14)$$

with  $\Omega_{\ell} = \sqrt{\omega_{\ell}^2 - \gamma_{\ell}^2/4}$ ,  $\omega_{\ell}^2 = \omega_1^2 + \ell\omega_{p, 1}^2/[(\epsilon_{\infty, 1} + 1) + 1]$ ,  $\tilde{\omega}_{\ell}^2 = \ell\omega_{p, 1}^2(2\ell+1)/[(\epsilon_{\infty} + 1) + 1]^2$ ,  $\Omega_s = \sqrt{\omega_s^2 - \gamma_s^2/4}$ ,  $\omega_s^2 = \omega_2^2 + \omega_{p, 2}^2/(\epsilon_{\infty, 2} + 1)$ , and  $\tilde{\omega}_s^2 = 2\omega_{p, 2}^2/(\epsilon_{\infty, 2} + 1)^2$ . Equations (13) and (14) illustrate that the surface responses are oscillatory, and the bound charges of the sphere and slab oscillate at eigenfrequencies  $\Omega_{\ell}$  and  $\Omega_s$  when displaced from equilibrium. The terms  $\tilde{\omega}_{\ell, s}$ , both proportional to the plasma frequencies  $\omega_{p, i}$ , encode the extent of the material's polarization. Comparing Eqs. (9) and (10) to a general solution for a damped, driven harmonic oscillator [32],  $x_0(t) = \int_{-\infty}^t dt' g_{\text{HO}}(t-t')F(t')/m_0$  (where  $g_{\text{HO}}$  is the harmonic oscillator Green's function), allows for extraction of the generalized forces which act upon coordinates  $u_{\ell m}$  and  $Q_n$ , defined as

$$F_{\ell m}(t) = -(2\ell+1) \int d\mathbf{x}' f_{\ell m}^*(\mathbf{x}') \rho(\mathbf{x}', t), \quad (15)$$

$$F_n(k, t) = -\frac{1}{k^2} \int d\mathbf{x}' \Lambda_n^*(k, \mathbf{x}') \rho(\mathbf{x}', t). \quad (16)$$

This permits the construction of the following equations of motion for the surface responses:

$$m_{\ell} \ddot{u}_{\ell m}(t) + m_{\ell} \gamma_{\ell} \dot{u}_{\ell m}(t) + m_{\ell} \omega_{\ell}^2 u_{\ell m}(t) = F_{\ell m}(t), \quad (17)$$

$$m_k \ddot{Q}_n(k, t) + m_k \gamma_2 \dot{Q}_n(k, t) + m_k \omega_s^2 Q_n(k, t) = F_n(k, t), \quad (18)$$

expressed in terms of the effective masses  $m_{\ell} = e^2/\sqrt{12\pi}a^3\tilde{\omega}_{\ell}^2$  and  $m_k = e^2k^2/\tilde{\omega}_s^2$ . From these equations, we see that the effective masses of the surface modes are inversely related to the material's charge carrier density, so as the polarizability of the object increases, the surface mode mass decreases. From Eqs. (15) and (16), we observe that the nature of the time-dependent generalized forces that act on  $m_{\ell}, m_k$  are determined by characteristics of the dielectric objects, their mode functions, and the perturbing charge distribution. We also take note that  $u_{\ell m}$  carries units of length (cm in cgs units), while  $Q_n$  is a coordinate density ( $\text{cm}^{-2}$ ), which illustrates that the surface mode responses of the sphere are localized and those of the slab are delocalized in space. Therefore, surface mode excitations of the sphere and slab in the IR region inherit the description of localized surface phonons (LSPs) and delocalized surface phonon (SPhs) [33], respectively.

### III. SYSTEM HAMILTONIAN AND COUPLED EQUATIONS OF MOTION

In the limit of no damping (i.e.,  $\gamma_{1,2} \rightarrow 0$ ), Eqs. (17) and (18) can be derived from the following Hamiltonians:

$$H_{\text{sph}} = \sum_{\ell m} \left[ \frac{p_{\ell m} p_{\ell m}^*}{m_{\ell}} + m_{\ell} \omega_{\ell}^2 u_{\ell m} u_{\ell m}^* - (F_{\ell m}^* u_{\ell m} + F_{\ell m} u_{\ell m}^*) \right], \quad (19)$$

$$H_{\text{slab}} = \sum_{n=-\infty}^{\infty} \int_0^{\infty} dk \left[ \frac{P_n P_n^*}{m_k} + m_k \omega_s^2 Q_n Q_n^* - (F_n^* Q_n + F_n Q_n^*) \right], \quad (20)$$

where  $p_{\ell m}$  and  $P_n$  are the momenta conjugate to the coordinates  $u_{\ell m}$  and  $Q_n$  for the sphere and semi-infinite slab surface modes. The total system Hamiltonian for the composite sphere-slab system in the presence of a uniformly moving electron is

$$H = H_{\text{el}}^0 + H_{\text{sph}}^0 + H_{\text{slab}}^0 + H_{\text{el, sph}} + H_{\text{el, slab}} + H_{\text{sph, slab}}. \quad (21)$$

In Eq. (21),  $H_{\text{el}}^0$  is the kinetic energy of the fast electron probe with charge density  $\rho_{\text{el}}(\mathbf{x}, t) = -e\delta(\mathbf{x} - \mathbf{r}_{\text{el}}(t))$ .  $H_{\text{sph}}^0$  and  $H_{\text{slab}}^0$  account for the internal energies of the dielectric objects, and  $H_{\text{el, sph}}$  and  $H_{\text{el, slab}}$  for the energy of interaction of the dielectrics with the fast electron. Finally,  $H_{\text{sph, slab}}$  accounts for the coupling energy between the dielectric bodies. For simplicity, we restrict the response of the sphere to the lowest order  $\ell = 1$  dipole mode and move from the spherical-multipole basis of Eq. (9) to Cartesian coordinates. The vector  $\mathbf{u}_0(t)$  defines the LSP coordinate with natural frequency  $\omega_0$ , effective mass  $m_0$ , and charge distribution  $\rho_0(\mathbf{x}, t) = -e\mathbf{u}_0(t) \cdot \nabla \delta(\mathbf{x} - \mathbf{r}_0)$ . Hamiltonians

for the individual dielectric objects are defined from Eq. (21) as

$$\begin{aligned} H_{\text{sph}} &= H_{\text{sph}}^0 + H_{\text{el,sph}} + H_{\text{sph,slab}} \\ &= \frac{\mathbf{p}_0^2}{2m_0} + \frac{1}{2}m_0\omega_0^2\mathbf{u}_0^2 - \mathbf{u}_0 \cdot \mathbf{F}_{\text{el}} + \int d\mathbf{x}\rho_0(\mathbf{x},t)\Phi_{\text{slab}}(\mathbf{x},t), \end{aligned} \quad (22)$$

$$\begin{aligned} H_{\text{slab}} &= H_{\text{slab}}^0 + H_{\text{el,slab}} + H_{\text{sph,slab}} \\ &= \sum_{n=-\infty}^{\infty} \int_0^{\infty} dk \left[ \frac{P_n P_n^*}{m_k} + m_k \omega_s^2 Q_n Q_n^* - (F_{\text{el},n}^* Q_n + F_{\text{el},n} Q_n^*) \right] + \int d\mathbf{x}\rho_0(\mathbf{x},t)\Phi_{\text{slab}}(\mathbf{x},t), \end{aligned} \quad (23)$$

where the energy of interaction between the LSPH and semi-infinite slab is calculated by integration of  $\rho_0$  with  $\Phi_{\text{slab}}$ .

Applying Hamilton's equations produces the following set of coupled Newton equations:

$$m_0\ddot{\mathbf{u}}_0(t) + m_0\gamma_1\dot{\mathbf{u}}_0(t) + m_0\omega_0^2\mathbf{u}_0 + e \sum_n \int_0^{\infty} dk Q_n(k,t) \nabla \Lambda_n(k, \mathbf{r}_0) = \mathbf{F}_{\text{el}}(t), \quad (24)$$

$$m_k\ddot{Q}_n(k,t) + m_k\gamma_2\dot{Q}_n(k,t) + m_k\omega_s^2 Q_n(k,t) + e\mathbf{u}_0(t) \cdot \nabla \Lambda_n(k, \mathbf{r}_0) = F_{\text{el},n}(k,t), \quad (25)$$

where dissipative forces have been reintroduced to provide a finite lifetime for the oscillatory responses.

We define the position vectors for the LSPH and the traveling electron coordinate as  $\mathbf{r}_0 = (0, h, 0)$  and  $\mathbf{r}_{\text{el}}(t) = (c, b, vt)$ .  $h$  is the height of the dipole above the slab surface,  $c$  is the displacement of the electron along the  $x$  axis,  $b$  is the electron's height above the dielectric slab's surface, and  $z = vt$  indicates that the electron is traveling along a  $z$ -oriented trajectory, with velocity  $v\hat{\mathbf{z}}$ , as represented in Fig. 1. The dynamics of the oscillatory LSPH are then governed by the integro-differential equation

$$\ddot{\mathbf{u}}_0(t) + \gamma_1\mathbf{u}_0(t)\omega_0^2\mathbf{u}_0(t) - \frac{e^2}{8m_0h^3} \int_{-\infty}^t dt' \zeta(t-t') [u_x(t')\hat{\mathbf{x}} + 2u_y(t')\hat{\mathbf{y}} + u_z(t')\hat{\mathbf{z}}] = \frac{\mathbf{F}_{\text{el}}(\mathbf{r}_0, t)}{m_0} + \int_{-\infty}^t dt' \zeta(t-t') \frac{\bar{\mathbf{F}}_{\text{el}}(\mathbf{r}_0, t')}{m_0}. \quad (26)$$

The terms  $\mathbf{F}_{\text{el}}(\mathbf{r}_0, t)$  and  $\bar{\mathbf{F}}_{\text{el}}(\mathbf{r}_0, t)$ , of which the latter is convolved with the surface response function of the dielectric slab, represent the forces on coordinate  $\mathbf{u}_0$  due to the evanescent field of the fast electron and the electron-induced surface charge on the slab, respectively. The latter term is commonly

referred to as the image field [34], defined as

$$\mathbf{F}_{\text{el}}(\mathbf{r}_0, t) = e^2 \frac{c\hat{\mathbf{x}} + (b-h)\hat{\mathbf{y}} + (vt)\hat{\mathbf{z}}}{[c^2 + (b-h)^2 + (vt)^2]^{\frac{3}{2}}}, \quad (27)$$

$$\bar{\mathbf{F}}_{\text{el}}(\mathbf{r}_0, t) = e^2 \frac{-c\hat{\mathbf{x}} + (b+h)\hat{\mathbf{y}} - (vt)\hat{\mathbf{z}}}{[c^2 + (b+h)^2 + (vt)^2]^{\frac{3}{2}}}. \quad (28)$$

From Eq. (26), the Fourier amplitude solutions  $\tilde{\mathbf{u}}_0(\omega)$  are determined via Fourier transformation

$$\tilde{u}_x(\omega) = \frac{\tilde{\alpha}_x(\omega)}{e^2} [\tilde{F}_{\text{el},x}(\mathbf{r}_0, \omega) + \tilde{\zeta}(\omega)\tilde{F}_{\text{el},x}(\mathbf{r}_0, \omega)], \quad (29)$$

$$\tilde{u}_y(\omega) = \frac{\tilde{\alpha}_y(\omega)}{e^2} [\tilde{F}_{\text{el},y}(\mathbf{r}_0, \omega) + \tilde{\zeta}(\omega)\tilde{F}_{\text{el},y}(\mathbf{r}_0, \omega)], \quad (30)$$

$$\tilde{u}_z(\omega) = \frac{\tilde{\alpha}_z(\omega)}{e^2} [\tilde{F}_{\text{el},z}(\mathbf{r}_0, \omega) + \tilde{\zeta}(\omega)\tilde{F}_{\text{el},z}(\mathbf{r}_0, \omega)], \quad (31)$$

and are expressed in terms of an effective polarizability  $\tilde{\alpha}_{x,y,z}$ , encoding the linear response of the LSPH coordinate and the external driving forces  $\tilde{F}_{\text{el},i}(\mathbf{r}_0, \omega)$  and  $\tilde{F}_{\text{el},i}(\mathbf{r}_0, \omega)$  regulating the response amplitude.

The second forcing term in Eqs. (29)–(31) implies that the frequency components of the electron's field will elicit a large image response when they coincide with the surface resonance conditions of the dielectric slab, magnifying the influence of  $\tilde{F}_{\text{el},i}(\mathbf{r}_0, \omega)$  on the resulting amplitude of  $\tilde{\mathbf{u}}_0(\omega)$ . Both forcing terms are defined by the Fourier transform of Eqs. (27) and

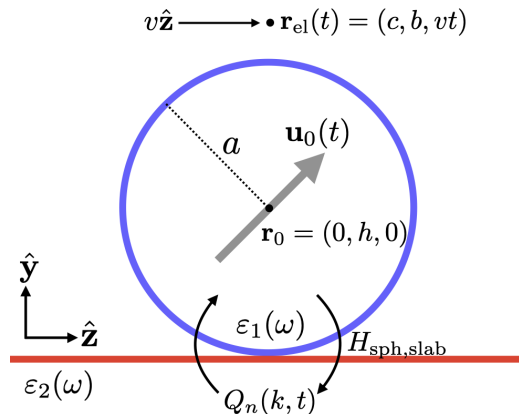


FIG. 1. Schematic of the composite sphere-slab dielectric system in the presence of a uniformly moving electron. Relevant parameters including the sphere radius  $a$ , the position of the electron  $\mathbf{r}_{\text{el}}(t)$ , and the time-dependent LSPH coordinate of the sphere  $\mathbf{u}_0$  at a fixed position  $\mathbf{r}_0$  are defined, along with the generalized coordinate of the substrate surface response  $Q_n(k, t)$  and the energy of interaction  $H_{\text{sph,slab}}$ . When the sphere rests directly on top of the slab, the height  $h = a$ .

(28), i.e.,

$$\begin{aligned}
 \tilde{F}_{\text{el},x}(\mathbf{r}_0, \omega) &= \frac{c}{R} \frac{2e^2|\omega|}{v^2} K_1\left(\frac{|\omega|R}{v}\right), \\
 \tilde{F}_{\text{el},x}(\mathbf{r}_0, \omega) &= -\frac{c}{\bar{R}} \frac{2e^2|\omega|}{v^2} K_1\left(\frac{|\omega|\bar{R}}{v}\right), \\
 \tilde{F}_{\text{el},y}(\mathbf{r}_0, \omega) &= \frac{b-h}{R} \frac{2e^2|\omega|}{v^2} K_1\left(\frac{|\omega|R}{v}\right), \\
 \tilde{F}_{\text{el},y}(\mathbf{r}_0, \omega) &= \frac{b+h}{\bar{R}} \frac{2e^2|\omega|}{v^2} K_1\left(\frac{|\omega|\bar{R}}{v}\right) \\
 \tilde{F}_{\text{el},z}(\mathbf{r}_0, \omega) &= \frac{2e^2\omega}{v^2} iK_0\left(\frac{|\omega|R}{v}\right), \\
 \tilde{F}_{\text{el},z}(\mathbf{r}_0, \omega) &= -\frac{2e^2\omega}{v^2} iK_0\left(\frac{|\omega|\bar{R}}{v}\right),
 \end{aligned} \quad (32)$$

determined with the aid of Basset's integral [35], where  $R = \sqrt{c^2 + (b-h)^2}$  and  $\bar{R} = \sqrt{c^2 + (b+h)^2}$ . The effective polarizabilities are defined as

$$\tilde{\alpha}_{x,z}(\omega) = \left[ \tilde{\alpha}(\omega)^{-1} - \frac{1}{8h^3} \tilde{\zeta}(\omega) \right]^{-1}, \quad (33)$$

$$\tilde{\alpha}_y(\omega) = \left[ \tilde{\alpha}(\omega)^{-1} - \frac{1}{4h^3} \tilde{\zeta}(\omega) \right]^{-1}, \quad (34)$$

where  $\tilde{\alpha}(\omega) = (e^2/m_0)(\omega_0^2 - \omega^2 - i\gamma_0\omega)^{-1}$  is the free space dynamic polarizability of the sphere. The modified polarizability terms  $\tilde{\alpha}_{x,y,z}$  account for the coupling of the LSPH to the LSPH induced surface response in the dielectric slab. The resulting pole structure of the modified polarizabilities describes the emergence of new normal mode resonance conditions when the proximity of the sphere and slab is varied.

The results detailed above are valid in the limit of  $d \gg a$  or when the dielectric slab can be safely modeled as semi-infinite. We now consider the case that the average radius of an interrogated sample is comparable to or significantly greater than the depth of the adjacent dielectric slab and generalize our results above to consider dielectric slabs of varying depths. We will demonstrate that even the presence of ultra thin planar dielectric surfaces may lead to nontrivial mode mixing with the dielectric sphere. Fortunately, this generalization is easily accomplished with an approach identical to that of the semi-infinite case. Solving for the Fourier amplitudes of the LSPH oscillations, considering the electron coordinate  $\mathbf{r}_{\text{el}}(t) = (0, b, vt)$ , we find

$$\tilde{u}_z(\omega) = \frac{\tilde{\alpha}_z(\omega)}{e^2} \left[ \tilde{F}_{\text{el},z}(\mathbf{r}_0, \omega) + \int_0^\infty dk \tilde{F}_{k,z}(\mathbf{r}_0, \omega) \tilde{\zeta}_k(\omega) \right], \quad (35)$$

$$\tilde{u}_y(\omega) = \frac{\tilde{\alpha}_y(\omega)}{e^2} \left[ \tilde{F}_{\text{el},y}(\mathbf{r}_0, \omega) + \int_0^\infty dk \tilde{F}_{k,y}(\mathbf{r}_0, \omega) \tilde{\zeta}_k(\omega) \right]. \quad (36)$$

The  $k$ -dependent force terms are proportional to the Fourier transform of the  $J_0(kvt)$  and  $J_1(kvt)$  cylindrical Bessel functions, where  $\tilde{\mathbf{F}}_k(\mathbf{r}_0, \omega) = \tilde{F}_{k,y}(\mathbf{r}_0, \omega)\hat{\mathbf{y}} + \tilde{F}_{k,z}(\mathbf{r}_0, \omega)\hat{\mathbf{z}}$  represents the force due to the electron-induced surface charge

on the finite slab, analogous to the semi-infinite case above. These terms are defined as

$$\tilde{F}_{k,z}(\mathbf{r}_0, \omega) = -i \frac{2e^2\omega}{v^2} \frac{e^{-k(b+h)}}{\sqrt{k^2 - \left(\frac{\omega}{v}\right)^2}} \quad \text{for } k \geq \frac{|\omega|}{v}, \quad (37)$$

$$\tilde{F}_{k,y}(\mathbf{r}_0, \omega) = \frac{2e^2}{v} \frac{k e^{-k(b+h)}}{\sqrt{k^2 - \left(\frac{\omega}{v}\right)^2}} \quad \text{for } k \geq \frac{|\omega|}{v}. \quad (38)$$

The effective polarizabilities in the case of the finite slab are

$$\tilde{\alpha}_z(\omega) = \left[ \tilde{\alpha}(\omega)^{-1} - \frac{1}{2} \int_0^\infty dk k^2 e^{-2kh} \tilde{\zeta}_k(\omega) \right]^{-1}, \quad (39)$$

$$\tilde{\alpha}_y(\omega) = \left[ \tilde{\alpha}(\omega)^{-1} - \int_0^\infty dk k^2 e^{-2kh} \tilde{\zeta}_k(\omega) \right]^{-1}. \quad (40)$$

In Fig. 2, we examine  $\text{Im } \tilde{\alpha}_y(\omega)$  as parameters  $d$  and  $h$  are varied, and show in the limit of  $d \rightarrow 0$  and  $h \gg a$  that its maxima coincide with the eigenspectrum of the decoupled surface modes of the sphere (blue line) and slab (red curves). The eigenvalues of the free space dielectric objects are provided by the poles of Eqs. (5) and (6), i.e.,

$$\tilde{\Omega}_\ell = -i \frac{\gamma_1}{2} \pm \Omega_\ell, \quad (41)$$

$$\tilde{\Omega}_\pm(k, d) = -i \frac{\gamma_2}{2} \pm \Omega_\pm, \quad (42)$$

$\Omega_0$  is the Fröhlich eigenfrequency [36] of the  $\ell = 1$  LSPH and  $\Omega_\pm = \sqrt{\omega_\pm^2(k, d) - (\gamma_2/2)^2}$  are the transverse (+) and longitudinal (−) Fuchs-Kliwiler (FK $_{\pm}$ ) eigenfrequencies [11,30]. The terms  $\omega_\pm^2(k, d) = \omega_2^2 + \omega_{p,2}^2/(\epsilon_\infty - a_\pm(k, d))$  are the natural frequencies of the oscillating FK $_{\pm}$  modes, where  $a_+(k, d) = (e^{-kd} + 1)(e^{-kd} - 1)^{-1}$  and  $a_-(k, d) = (e^{-kd} - 1)(e^{-kd} + 1)^{-1}$ . As  $d \rightarrow \infty$ ,  $\Omega_\pm \rightarrow \Omega_s$ , and the FK $_{\pm}$  modes become energetically degenerate. This results in only one remaining resonance for the semi-infinite slab, as predicted in Eq. (14). Also, Eqs. (35)–(40) reduce to Eqs. (29)–(34) in this limit.

Figure 2(a) displays  $\text{Im } \tilde{\alpha}_y(\omega)$  as the sphere approaches a 100-nm-thick slab of the same dielectric composition, clearly displaying mode splitting beginning near  $h \sim 2a$  that is maximized at  $h = a$ . With  $h = a$  fixed, Fig. 2(b) shows the result of decreasing the substrate thickness from 100 nm to 0 nm. Here we see that the splitting between the FK $_{\pm}$  modes is greatest as the slab becomes increasingly thin, although the contribution to  $\text{Im } \tilde{\alpha}_y(\omega)$  from the transverse FK $_+$  mode is rapidly diminished. At  $d = 0$  nm, contributions from the FK $_{\pm}$  modes disappear from  $\text{Im } \tilde{\alpha}_y(\omega)$  altogether, as expected. When  $d$  is decreased from  $2a \geq d > 0$  nm, three peaks emerge in  $\text{Im } \tilde{\alpha}_y(\omega)$ , indicating three normal mode resonances due to mixing of the sphere's LSPH mode with the FK $_{\pm}$  modes of the slab. Figure 2(c) highlights in the regime of  $0 < d \leq a$  how the normal mode responses of the dimer dissociate to the free space normal mode responses of the decoupled sphere and slab. In the regime of  $2a < d \leq 100$  nm, we notice the formation of two normal modes in  $\text{Im } \tilde{\alpha}_y(\omega)$ , as the participating FK $_{\pm}$  modes unite from two energetically distinct surface mode resonances into one. Also, as the slab depth increases, its one remaining surface mode resonance more effectively couples to the LSPH, as evidenced by the

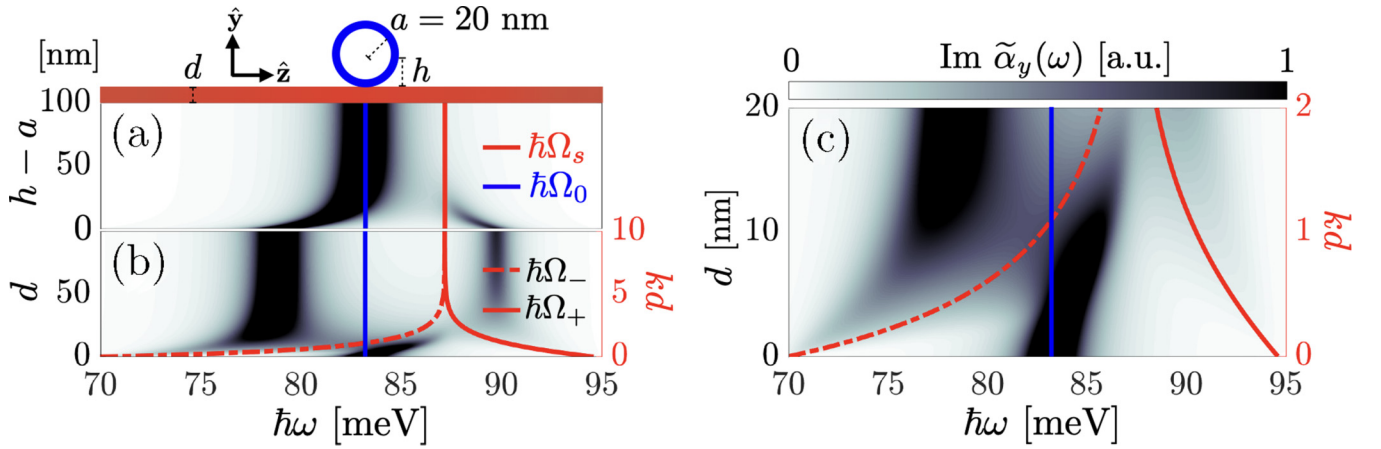


FIG. 2. Evolution of  $\text{Im } \tilde{\alpha}_y(\omega)$  for an  $a = 20$  nm sphere when the sphere height ( $h$ ) and the slab depth ( $d$ ) are varied. The dielectric response of the sphere and slab are defined by a common Lorentz oscillator dielectric function [i.e.,  $\tilde{\epsilon}_1(\omega) = \tilde{\epsilon}_2(\omega)$ ], parametrized to the bulk response of MgO. In panel (a), the sphere is moon-landed onto a 100-nm-thick slab from an initial distance of 100 nm between the sphere and the slab surfaces. In panel (b), the depth of the slab is decreased from  $d = 100$  nm to 0 nm, and the  $\text{FK}_{\pm}$  ( $\hbar\Omega_{\pm}$ ) modes are allowed to evolve as  $kd$  is varied.  $\Omega_0$  is the  $\ell = 1$  eigenfrequency of the free-space sphere (blue line) and  $\Omega_s$  is the eigenfrequency of the free-space semi-infinite slab (red curves). Panel (c) provides a closer examination of the mixed surface mode responses in the region of  $0 \leq d \leq a$ . We observe that as the slab depth becomes increasingly small, the normal mode responses resolve to the free-space eigenfrequencies.

increase in amplitude of the higher energy 90 meV branch for  $d > 2a$  in Fig. 2(b). This result is expected due to the increased amount of polarizable material proximal to the LSPH, leading to a larger effective coupling between the dielectric bodies.

#### IV. INELASTIC SCATTERING PROBABILITY FOR THE COMPOSITE SPHERE-SLAB SYSTEM

To derive the inelastic scattering probability of the composite system, we first consider the time-averaged work performed on a passing electron by an external field using Poynting's theorem. The average work  $\Delta E$  is equivalent to the first energy moment of the inelastic scattering probability

function  $\Gamma(\omega)$  according to [37]

$$\begin{aligned} \Delta E &= \int d\mathbf{x} dt \mathbf{E}_{\text{ind}}(\mathbf{x}, t) \cdot \mathbf{J}_{\text{el}}(\mathbf{x}, t) \\ &= \int d(\hbar\omega) \hbar\omega \Gamma(\omega). \end{aligned} \quad (43)$$

Making use of the continuity equation, Eq. (43) yields  $\Gamma(\omega) = (\pi \hbar^2)^{-1} \int d\mathbf{x} \text{Im}\{\tilde{\rho}_{\text{el}}^*(\mathbf{x}, \omega) \Phi_{\text{ind}}(\mathbf{x}, \omega)\}$  under the quasistatic approximation. In the case of the composite dielectric sphere-slab structure, where the total induced potential in the vacuum region above the dielectric slab is  $\tilde{\Phi}_{\text{ind}} = \tilde{\Phi}_{\text{sph}} + \tilde{\Phi}_{\text{slab}}$ , the resulting loss probability for the aloof parallel-grazing trajectory depicted in Figs. 1 and 3 is

$$\Gamma(\omega) = \lim_{z_0 \rightarrow \infty} \frac{2z_0}{\pi} \left( \frac{e}{\hbar v} \right)^2 \int_{\omega/v}^{\infty} dk \frac{e^{-2kb}}{\sqrt{k^2 - (\frac{\omega}{v})^2}} \text{Im}\{\tilde{\zeta}_k(\omega)\} + \frac{1}{\pi \hbar^2} \text{Im}\left\{ \tilde{\mathbf{u}}_0(\omega) \cdot \left[ \tilde{\mathbf{F}}_{\text{el}}(\mathbf{r}_0, \omega) + \int_0^{\infty} dk \tilde{\zeta}_k^*(\omega) \tilde{\mathbf{F}}_k(\mathbf{r}_0, \omega) \right]^* \right\}. \quad (44)$$

Again, in the limit that the depth of the dielectric slab  $d \rightarrow \infty$ , Eq. (44) reduces to

$$\Gamma(\omega) = \lim_{z_0 \rightarrow \infty} \frac{2z_0}{\pi} \left( \frac{e}{\hbar v} \right)^2 K_0 \left( \frac{2\omega b}{v} \right) \text{Im}\{\tilde{\zeta}(\omega)\} + \frac{1}{\pi \hbar^2} \text{Im}\left\{ \tilde{\mathbf{u}}_0(\omega) \cdot \left[ \tilde{\mathbf{F}}_{\text{el}}(\mathbf{r}_0, \omega) + \tilde{\zeta}^*(\omega) \tilde{\mathbf{F}}_{\text{el}}(\mathbf{r}_0, \omega) \right]^* \right\}. \quad (45)$$

In either case, the first terms described under the limit  $z_0 \rightarrow \infty$ , where  $z_0$  is the path length traveled by the electron, were originally derived by Takimoto, Echenique, Rivacoba, and Pendry (TERP), and again recently reported by Echarri *et al.* in the case of swift electrons interacting with atomically thin surfaces, traveling along parallel trajectories [34,38–41]. We will refer to the thin film scattering probability as  $\Gamma_{\text{TERP}}$ , and it accounts for the contribution to the total scattering probability  $\Gamma(\omega)$  from the probing electron's interaction with the electron-induced wake potential on the slab [42]. The

second term  $\propto \text{Im}\{\tilde{\mathbf{u}}_0(\omega) \cdot \tilde{\mathbf{F}}_{\text{el}}^*(\mathbf{r}_0, \omega)\}$  accounts for its interaction with the LSPH mode, while the final term  $\propto \text{Im}\{\tilde{\mathbf{u}}_0(\omega) \cdot [\int_0^{\infty} dk \tilde{\zeta}_k^*(\omega) \tilde{\mathbf{F}}_k(\mathbf{r}_0, \omega)]^*\}$  relays the fast electron's interaction with the LSPH-induced surface mode on the slab. The first term of Eq. (44),  $\Gamma_{\text{TERP}}$ , is devoid of any information concerning coupling between the surface modes of the dielectric sphere and slab, and is equivalent to the loss probability of an isolated thin film. Therefore, we regard it as a background signal only and proceed with an evaluation of  $\Gamma - \Gamma_{\text{TERP}}$

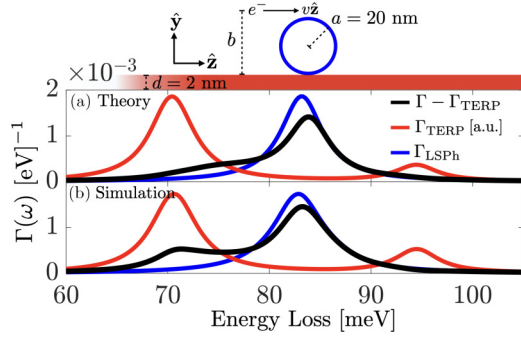


FIG. 3. Comparison of (a) Eq. (44) to (b) simulation for the monomers (free space sphere and slab), and the dimer (composite sphere-slab system) after background subtraction. For the simulated composite system, the numerical scattering probability for a  $d = 2$  nm dielectric slab is subtracted from the result for a composite  $a = 20$  nm sphere positioned on top of a slab of identical dimensions. A Lorentz oscillator dielectric function parametrized to the bulk response of MgO is used to describe the material responses of the sphere and slab. The electron beam height is  $b = 3a$ , traveling uniformly with 10 keV of kinetic energy, and the location of the charge distributions are defined by  $\mathbf{r}_0 = (0, a, 0)$  and  $\mathbf{r}_{el} = (0, b, vt)$  for the sphere and probe, respectively. In both simulation and theory,  $\Gamma_{\text{TERP}}$  is normalized to  $\Gamma_{\text{LSPh}}$ .

when comparing our analytic results in Fig. 3(a) to simulated scattering experiments in Fig. 3(b).

To test the validity of the analytic loss function in Eq. (44), we have performed fully retarded numerical electrodynamics simulations using the electron-driven discrete dipole approximation ( $e$ -DDA) method [43,44] on finite, cylindrical dielectric slabs, 2 nm in depth and 400 nm in width, with a parallel-grazing, nonpenetrating trajectory, and collected the corresponding scattering probability spectrum. An additional simulation was performed on a dielectric slab of identical dimensions but in the presence of a dielectric sphere with a radius of 20 nm positioned directly on top of the slab. In each case, the simulations were performed with an interdipole spacing of 1 nm, and with an electron velocity of 10 keV. The spectrum for the isolated slab is treated as a background and is subtracted from the scattering probability of the composite system. For the isolated slab, we observe the response of longitudinal (FK<sub>-</sub>, 70 meV) and transverse (FK<sub>+</sub>, 94 meV) Fuchs-Kliewer modes, showcasing that the finite-sized simulated slab hosts normal mode responses at energies similar to those predicted by the eigenspectrum displayed in Fig. 2. This is observed analytically via  $\Gamma_{\text{TERP}}$ , in Fig. 3(a), which predicts energy loss by the passing electron when it couples to the FK<sub>±</sub>-modes of the  $d = 2$  nm slab.

In the case of the sphere-slab dimer's scattering probability, in both theory and simulation, we notice a slight deviation from the scattering spectrum of the independent dielectric objects. This includes a blueshifting of the peak associated with  $\Gamma_{\text{LSPh}}$  (84 meV) and a blueshift in the peak associated with the FK<sub>-</sub> mode (72 meV). And although its contribution to  $\Gamma - \Gamma_{\text{TERP}}$  is subtle, we observe a redshift in the peak associated with the FK<sub>+</sub> mode of the slab (92 meV), indicating the formation of new normal modes in the composite system as a result of induced near-field coupling between the dielectric ob-

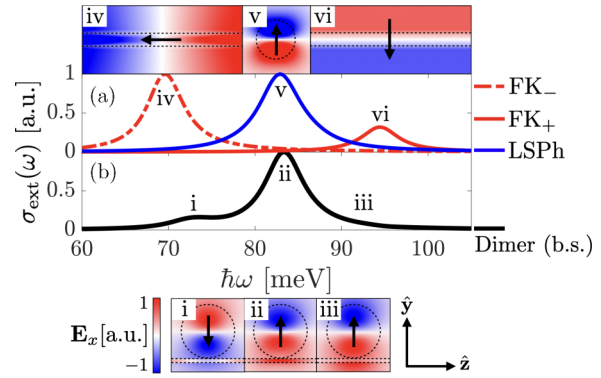


FIG. 4. Normal component ( $\mathbf{E}_x$ ) induced electric field contour maps for the independent sphere and slab (a) under  $y$  and  $z$ -polarized plane-wave illumination and the composite sphere-slab system under  $y$ -polarized plane-wave illumination (b). The fields are evaluated at the associated peaks of the extinction spectrum (i)–(vi) to illustrate the near-field coupling between the sphere and the slab (i)–(iii) and to examine the induced field profile of the free space monomers, namely, the transverse and longitudinal surface modes hosted by the dielectric slab (iv), (vi) and the dipolar surface modes of the sphere (v).

jects. Additionally, the composite loss probability suffers a decrease in intensity relative to that of the free space sphere due to coupling of the LSPH to its own induced surface response on the slab and the traveling electron's wake potential [42].

In both theory and simulation, we have utilized a Lorentz oscillator dielectric function, parametrized to the bulk vibrational response of MgO, a material whose local dielectric function has been well characterized via thin film ellipsometry [45,46] in the near IR. In addition, the bulk and surface vibrational mode excitations for MgO nanoparticles of varying morphologies have been extensively characterized in recent electron scattering experiments, lattice dynamics calculations, and molecular dynamics simulations [16,47]. While our theoretical model is general enough for characterizing any combination of dielectric materials for the sphere and slab under a quasistatic approximation, MgO was selected due to it hosting a discrete bulk response in the far IR [45], which lends itself well to a simple fitting procedure for the Lorentz-oscillator dielectric parameters. Also, the resulting surface modes are nearly co-resonant between the sphere and the slab when they are composed of the same dielectric material, which leads to increased mode mixing. Herein, we use the following dielectric parameter values  $\epsilon_\infty = 2$ ,  $\hbar\gamma_{1,2} = 5$  meV,  $\hbar\omega_{1,2} = 70$  meV, and  $\hbar\omega_p = 90$  meV for MgO.

To inspect the near-field interaction of the LSPH mode with the FK<sub>±</sub> modes, we calculate background subtracted plane-wave extinction spectra [48] for the dimer in a manner identical to that of the background subtracted scattering probability, with the polarization of the incident electric field oriented normal to the surface of the slab. For comparison, extinction calculations for the individual monomers are also presented. Figure 4 displays the normal component of the induced electric field at the sphere-vacuum interface for both the composite (dimer) system (i)–(iii) and for the individual

monomers (iv–vi) at the associated peak energies in the extinction spectrum.

First, examining the response of the monomer dielectric objects, plane-wave excitation of the isolated sphere Fig. 4(v) drives the LSP mode, irrespective of the orientation of incident polarization. Extinction measurements of the dielectric slab, however, reveal a highly biased response between polarization of the incident field parallel and normal to the slab surface. For the chosen configuration, a  $y$ -polarized plane-wave source selects the slab's transverse  $FK_+$  mode [Fig. 4(vi)] while  $z$  polarization along the long axis of the slab drives the longitudinal  $FK_-$  mode [Fig. 4(iv)]. For the dimer, excitation energy [Fig. 4(i), 72 meV] reveals an out-of-phase oscillation of the LSP, indicated by the change in orientation of the dipolar-field relative to the field profile at energy [Fig. 4(ii), 84 meV]. This indicates that the LSP dipole oriented normal to the slab's surface appreciably couples to the  $FK_-$  mode of the slab, while the vanishingly small peak at [Fig. 4(iii), 93 meV] suggests a weak coupling between the LSP and the slab's  $FK_+$  mode. The degree of coupling between the surface modes is evident in the surface plot of  $\text{Im } \tilde{\alpha}_y(\omega)$ , as the resonant peak associated with the dipole begins to shift upon approach to the slab's surface, along with the emerging influence of the slab's  $FK_-$  mode in the modified response function of the LSP. This coupling of the surface modes is also reflected in both the simulated plane-wave extinction calculations, and in the scattering probability profile produced by theory and simulation. This is demonstrated in Figs. 2–4 when comparing the resonant frequencies of the free space dielectric objects to those of the background subtracted dimer, both at the level of the spectroscopic observables and at the level of the response function  $\tilde{\alpha}_y(\omega)$ .

In both electron scattering and plane wave extinction simulations, we have restricted the dimensions of the substrate to a shallow depth of  $d = 2$  nm. This was due to computational restrictions concerning the size of the interrogated dielectric structures. Specifically, we considered the necessity of extending the slab in width to dimensions large enough to observe the response of the  $FK_{\pm}$  modes in the simulated scattering probability, while remaining in good agreement with  $\Gamma_{\text{TERP}}$  in Fig. 3(a).

## V. CONCLUSION

As the spectroscopic range of modern EEL measurements have expanded into the far-IR, the vibrational resonances of dielectric materials are now susceptible to detailed characterization via inelastic electron scattering spectroscopy. Recent advances in electron energy monochromation and aberration correction have laid bare the need to investigate the influence of the resonant dielectric environment on the sample's loss probability in the IR region. Of particular importance is the influence of dielectric substrates which support dielectric nanoparticle targets in typical EELS experiments, which at low energy may inherit the role of an active dynamical contributor to the resulting signal. Although, in typical electron-scattering experiments, an electron probe geometry which penetrates the supporting substrate is more commonly

employed, the modified surface response functions derived within encode the spectral features of the new normal mode resonances of the sphere-slab dimer, which are independent of orientation of the electron probe's trajectory. Common substrates composed of both amorphous oxide and ionic crystalline materials are typically nondispersive in the optical regime but often host a rich set of surface vibrational responses at thermal energies. While the inelastic scattering of fast electrons by isolated thin films and isolated nanoparticle targets of varying morphology have been extensively studied and rigorously modeled, under both radiative and nonradiative approximations, an in-depth description of how a dispersive, resonant substrate influences the loss probability of the target specimen has so far not been made. This has motivated us to construct a theoretical model detailing the contributions to the EELS observable due to induced near-field coupling in a composite particle-slab assembly.

To accomplish this, we considered the case of a spherical dielectric nanoparticle adjacent to a dielectric slab of varying depths. We defined generalized coordinates and effective masses for the surface modes of the dielectric objects in terms of their bulk dielectric parameters, along with the generalized forces which drive the surface modes. Determining the energy of interaction between the sphere and the slab allowed us to construct coupled equations of motion, from which we extracted the modified linear response function of the lowest order  $\ell = 1$  LSP mode of the dielectric sphere. Then, forcing the coupled system with a fast electron moving parallel to the slab's surface and external to the dielectric objects, we derived an analytic expression for the resulting inelastic scattering probability  $\Gamma$  of the dimer. Comparison between our analytic results and numerical electrodynamics simulations demonstrate excellent agreement, both under electron beam and plane-wave excitation. Taken together, this work has revealed that when target and substrate surface modes are coresonant, the effects of the substrate's presence are nontrivial in the observed spectroscopic observable and may substantially modify the apparent response of the target specimen. Thus, careful theoretical analysis like that presented herein is required to interpret the measured scattering signal. Additionally, this study offers fundamental insights into the physical origin of the scattering signal in composite systems, which is relevant for quantitative analysis of nanoscale physical properties such as phonon mapping [15], local temperature measurement [14], and the phonon density of states [11].

## ACKNOWLEDGMENTS

The authors acknowledge stimulating discussions with Kevin C. Smith on the interpretation and analysis of the modified linear response functions appearing in Eqs. (39) and (40). Work at the University of Washington was supported by the U.S. Department of Energy (DOE), Office of Science, Office of Basic Energy Sciences (BES), Materials Sciences and Engineering Division under Award No. DE-SC0018040 (E.K.B., D.J.M.). M.J.L. acknowledges the financial support of a Discovery Grant from NSERC.

- [1] O. L. Krivanek, T. C. Lovejoy, M. F. Murfitt, G. Skone, P. E. Batson, and N. Dellby, Towards sub-10 meV energy resolution STEM-EELS, *J. Phys.: Conf. Ser.* **522**, 012023 (2014).
- [2] O. L. Krivanek, T. C. Lovejoy, N. Dellby, T. Aoki, R. Carpenter, P. Rez, E. Soignard, J. Zhu, P. E. Batson, and M. J. Lagos, Vibrational spectroscopy in the electron microscope, *Nature (London)* **514**, 209 (2014).
- [3] O. L. Krivanek, T. C. Lovejoy, N. J. Bacon, G. J. Corbin, N. Dellby, P. Hrnčirik, M. F. Murfitt, G. Skone, Z. S. Szilagy, and P. E. Batson, High energy resolution monochromated EELS-STEM system, *Microsc. Microanal.* **19**, 1124 (2013).
- [4] J. A. Hachtel, A. R. Lupini, and J. C. Idrobo, Exploring the capabilities of monochromated electron energy loss spectroscopy in the infrared regime, *Sci. Rep.* **8**, 1 (2018).
- [5] P. Tiemeijer, M. Bischoff, B. Freitag, and C. Kisielowski, Using a monochromator to improve the resolution in tem to below 0.5 Å. part i: Creating highly coherent monochromated illumination, *Ultramicroscopy* **114**, 72 (2012).
- [6] P. E. Batson, N. Dellby, and O. L. Krivanek, Sub-Ångstrom resolution using aberration corrected electron optics, *Nature (London)* **418**, 617 (2002).
- [7] P. Rez, T. Aoki, K. March, D. Gur, O. L. Krivanek, N. Dellby, T. C. Lovejoy, S. G. Wolf, and H. Cohen, Damage-free vibrational spectroscopy of biological materials in the electron microscope, *Nat. Commun.* **7**, 10945 (2016).
- [8] D. M. Haiber and P. A. Crozier, Nanoscale probing of local hydrogen heterogeneity in disordered carbon nitrides with vibrational electron energy-loss spectroscopy, *ACS Nano* **12**, 5463 (2018).
- [9] U. Hohenester, A. Trügler, P. E. Batson, and M. J. Lagos, Inelastic vibrational bulk and surface losses of swift electrons in ionic nanostructures, *Phys. Rev. B* **97**, 165418 (2018).
- [10] K. Venkatraman, B. D. Levin, K. March, P. Rez, and P. A. Crozier, Vibrational spectroscopy at atomic resolution with electron impact scattering, *Nat. Phys.* **15**, 1237 (2019).
- [11] H. Lourenço-Martins and M. Kociak, Vibrational Surface Electron-Energy-Loss Spectroscopy Probes Confined Surface-Phonon Modes, *Phys. Rev. X* **7**, 041059 (2017).
- [12] P. A. Crozier, Vibrational and valence aloof beam EELS: A potential tool for nondestructive characterization of nanoparticle surfaces, *Ultramicroscopy* **180**, 104 (2017).
- [13] C. Dwyer, T. Aoki, P. Rez, S. L. Y. Chang, T. C. Lovejoy, and O. L. Krivanek, Electron-Beam Mapping of Vibrational Modes with Nanometer Spatial resolution, *Phys. Rev. Lett.* **117**, 256101 (2016).
- [14] M. J. Lagos and P. E. Batson, Thermometry with subnanometer resolution in the electron microscope using the principle of detailed balancing, *Nano Lett.* **18**, 4556 (2018).
- [15] M. J. Lagos, A. Trügler, U. Hohenester, and P. E. Batson, Mapping vibrational surface and bulk modes in a single nanocube, *Nature (London)* **543**, 529 (2017).
- [16] M. J. Lagos, A. Trügler, V. Amarasinghe, L. C. Feldman, U. Hohenester, and P. E. Batson, Excitation of long-wavelength surface optical vibrational modes in films, cubes and film/cube composite system using an atom-sized electron beam, *Microscopy* **67**, 3 (2018).
- [17] X. Yan, C. Liu, C. A. Gadre, L. Gu, T. Aoki, T. C. Lovejoy, N. Dellby, O. L. Krivanek, D. G. Schlom, and R. Wu, Single-defect phonons imaged by electron microscopy, *Nature (London)* **589**, 65 (2021).
- [18] A. Pinchuk, A. Hilger, G. von Plessen, and U. Kreibig, Substrate effect on the optical response of silver nanoparticles, *Nanotechnology* **15**, 1890 (2004).
- [19] C. Cherqui, G. Li, J. A. Busche, S. C. Quillin, J. P. Camden, and D. J. Masiello, Multipolar nanocube plasmon mode-mixing in finite substrates, *J. Phys. Chem. Lett.* **9**, 504 (2018).
- [20] S. Kakhodazadeh, T. Christensen, M. Beleggia, N. A. Mortensen, and J. B. Wagner, The substrate effect in electron energy-loss spectroscopy of localized surface plasmons in gold and silver nanoparticles, *ACS Photon.* **4**, 251 (2017).
- [21] G. Li, C. Cherqui, N. W. Bigelow, G. Duscher, P. J. Straney, J. E. Millstone, D. J. Masiello, and J. P. Camden, Spatially mapping energy transfer from single plasmonic particles to semiconductor substrates via STEM/EELS, *Nano Lett.* **15**, 3465 (2015).
- [22] Y. Fujiyoshi, T. Nemoto, and H. Kurata, Substrate effects on LSP of a truncated silver nano-sphere observed by EELS, *Microscopy* **64**, i99 (2015).
- [23] Y. Fujiyoshi, T. Nemoto, and H. Kurata, Studying substrate effects on localized surface plasmons in an individual silver nanoparticle using electron energy-loss spectroscopy, *Ultramicroscopy* **175**, 116 (2017).
- [24] D. Kordahl and C. Dwyer, Enhanced vibrational electron energy-loss spectroscopy of adsorbate molecules, *Phys. Rev. B* **99**, 104110 (2019).
- [25] S. Griffin, N. P. Montoni, G. Li, P. J. Straney, J. E. Millstone, D. J. Masiello, and J. P. Camden, Imaging energy transfer in Pt-decorated au nanoprisms via electron energy-loss spectroscopy, *J. Phys. Chem. Lett.* **7**, 3825 (2016).
- [26] S. C. Quillin, C. Cherqui, N. P. Montoni, G. Li, J. P. Camden, and D. J. Masiello, Imaging plasmon hybridization in metal nanoparticle aggregates with electron energy-loss spectroscopy, *J. Phys. Chem. C* **120**, 20852 (2016).
- [27] J. Schwinger, L. L. DeRaad Jr, K. Milton, and W.-Y. Tsai, *Classical Electrodynamics* (Westview Press, Nashville, TN, 1998).
- [28] K. Cahill, Models of membrane electrostatics, *Phys. Rev. E* **85**, 051921 (2012).
- [29] H. S. Cohl and J. E. Tohline, A compact cylindrical Green's function expansion for the solution of potential problems, *Astrophys. J.* **527**, 86 (1999).
- [30] R. Fuchs and K. Kliewer, Optical modes of vibration in an ionic crystal slab, *Phys. Rev.* **140**, A2076 (1965).
- [31] C. Cherqui, N. Thakkar, G. Li, J. P. Camden, and D. J. Masiello, Characterizing localized surface plasmons using electron energy-loss spectroscopy, *Annu. Rev. Phys. Chem.* **67**, 331 (2016).
- [32] F. W. Byron and R. W. Fuller, *Mathematics of Classical and Quantum Physics* (Courier Corporation, North Chelmsford, MA, 2012).
- [33] D. Mills and E. Burstein, Polaritons: The electromagnetic modes of media, *Rep. Prog. Phys.* **37**, 817 (1974).
- [34] A. Rivacoba, N. Zabala, and J. Aizpurua, Image potential in scanning transmission electron microscopy, *Prog. Surf. Sci.* **65**, 1 (2000).
- [35] M. Abramowitz and I. A. Stegun, *Handbook of Mathematical Functions with Formulas, Graphs, and Mathematical Tables* (US Government Printing Office, Washington, DC, 1948), Vol. 55.
- [36] H. Fröhlich, *Theory of Dielectrics: Dielectric Constant and Dielectric Loss* (Oxford University Press, Oxford, UK, 1958), Vol. 190.

- [37] R. H. Ritchie, Plasma losses by fast electrons in thin films, *Phys. Rev.* **106**, 874 (1957).
- [38] N. Takimoto, Plasmon excitation by charged particles outside a metal film, *Phys. Rev.* **146**, 366 (1966).
- [39] P. Echenique and J. Pendry, Absorption profile at surfaces, *J. Phys. C* **8**, 2936 (1975).
- [40] A. R. Echarri, J. D. Cox, and F. J. García de Abajo, Quantum effects in the acoustic plasmons of atomically thin heterostructures, *Optica* **6**, 630 (2019).
- [41] A. Rodríguez Echarri, E. J. H. Skjølstrup, T. G. Pedersen, and F. J. García de Abajo, Theory of electron energy-loss spectroscopy in atomically thin metallic films, *Phys. Rev. Res.* **2**, 023096 (2020).
- [42] F. J. García de Abajo and P. M. Echenique, Wake potential in the vicinity of a surface, *Phys. Rev. B* **46**, 2663 (1992).
- [43] N. W. Bigelow, A. Vaschillo, V. Iberi, J. P. Camden, and D. J. Masiello, Characterization of the electron- and photon-driven plasmonic excitations of metal nanorods, *ACS Nano* **6**, 7497 (2012).
- [44] N. W. Bigelow, A. Vaschillo, J. P. Camden, and D. J. Masiello, Signatures of Fano interferences in the electron energy loss spectroscopy and cathodoluminescence of symmetry-broken nanorod dimers, *ACS Nano* **7**, 4511 (2013).
- [45] E. D. Palik, *Handbook of Optical Constants of Solids* (Academic Press, Cambridge, MA, 1998), Vol. 3.
- [46] A. Hofmeister, E. Keppel, and A. Speck, Absorption and reflection infrared spectra of MgO and other diatomic compounds, *Mon. Not. R. Astron. Soc.* **345**, 16 (2003).
- [47] L. Marks, Observation of the image force for fast electrons near an MgO surface, *Solid State Commun.* **43**, 727 (1982).
- [48] B. T. Draine and P. J. Flatau, Discrete-dipole approximation for scattering calculations, *J. Opt. Soc. Am. A* **11**, 1491 (1994).